

Transport properties of doped permalloy via ab-initio calculations: effect of the host disorder

O. Šipr,^{1,2,*} S. Wimmer,³ S. Mankovsky,³ and H. Ebert³

¹*Institute of Physics of the Czech Academy of Sciences,
Cukrovarnická 10, CZ-162 53 Prague, Czech Republic*

²*New Technologies Research Centre, University of West Bohemia, CZ-301 00 Pilsen, Czech Republic*

³*Universität München, Department Chemie, Butenandtstr. 5-13, D-81377 München, Germany*

(Dated: June 21, 2021)

Transport properties of permalloy doped with V, Co, Pt, and Au are explored via ab-initio calculations. For this purpose, the Kubo-Bastin formula is evaluated within the fully relativistic Korringa-Kohn-Rostoker Green function formalism. Finite temperature effects are treated by means of the alloy analogy model. It is shown that the fact that the host is disordered and not crystalline has a profound effect on how the conductivities characterizing the anomalous Hall effect and the spin Hall effect depend on the dopant concentration. Several relationships between quantities characterizing charge and spin transport are highlighted. The rate of decrease of the longitudinal charge conductivity with increasing doping depends on the dopant type, following the sequence Co–Au–Pt–V. The dependence of the anomalous Hall and spin Hall conductivities on the dopant concentration is found to be non-monotonic. Introducing a finite temperature changes the overall trends significantly. The theoretical results are compared with available experimental data.

I. INTRODUCTION

There have been growing efforts to complement conventional electronics, based on manipulating conducting electrons via charge, by spintronics, which manipulates the electron spin. A prominent role is played in this respect by transport phenomena closely linked to the spin orbit coupling (SOC), such as the anomalous Hall effect (AHE), the spin Hall effect (SHE), or the anisotropic magnetoresistance (AMR). Intimately connected with the development of spintronics is the search for corresponding new materials. The modification of magnetic materials by doping is a promising and intensively studied way to make progress. Transport properties can be strongly influenced even by very low dopant concentrations. Understanding the underlying mechanisms responsible for the modification of transport properties is thus very important. A reliable ab-initio description of the way doping affects transport phenomena is a necessary part of this process.

So far the theoretical description in the field has focused mostly on how doping influences transport properties of crystalline, i.e., clean systems. Concepts and intuitive views have been established that can be conveniently used when interpreting experiments [1–3]. However, experimental and technological interest is turning also to alloys which offer a diverse range of properties. The question is to what extent the approaches that proved to be useful for doped crystals can be transferred to doped alloys. To start with, one of the key factors affecting theoretical analysis of transport in doped crystals is that the longitudinal charge conductivity tends to infinity for zero doping (for $T=0$ K). This is no longer true if the host is a disordered alloy. So one can presume that some trends of the transport properties with doping which are common and well understood for crystalline

hosts will not occur for doped alloys.

One of the widely studied chemically disordered materials is permalloy $\text{Fe}_{19}\text{Ni}_{81}$. It is attractive because of its high magnetic permeability but also because of its transport properties, which are characterized by a high and low electrical conductivity in the majority and minority spin channels, respectively. Several studies how permalloy (Py) properties can be modified via doping by magnetic or non-magnetic atoms were published recently [4–11].

The aim of this study is to investigate transport properties of doped Py via ab-initio calculations, for zero and finite temperatures alike. Special attention is paid to understanding the trends with the doping and to how this compares with trends for crystalline hosts. Apart from the longitudinal conductivity, we focus on the SOC-related phenomena AHE, SHE, and AMR. The dopants we consider are V, Co, Pt, and Au. In this way we cover a wide range of circumstances: E.g., Co is magnetic, V and Pt are non-magnetic but easily polarizable, Au is non-magnetic and hard to polarize. The induced magnetic moment of V and Pt is oriented antiparallel and parallel, respectively, to the magnetization of the Py host. The SOC is weak at V and Co but strong at Pt and Au. Co lies between Fe and Ni in the periodic table, so it will presumably not disturb the electronic structure of Py much while the other dopants should pose a substantial disturbance.

By performing ab-initio calculations and analyzing our results, we will show that the fact that the Py host is disordered and not crystalline has profound influence on the dependence of the AHE and SHE on the dopant concentration. In particular, this dependence cannot be ascribed unambiguously to skew scattering, side-jump scattering, or intrinsic contributions in the same way as it can be done when investigating the effect of doping for an ordered crystalline host. Where possible, our theoretical

results are compared with available experimental data.

II. THEORETICAL SCHEME

A. Charge and spin conductivities

The charge and spin conductivities are calculated in a linear-response regime, using a particular form of

$$\mathcal{C}_{\mu\nu} = \mathcal{C}_{\mu\nu}^I + \mathcal{C}_{\mu\nu}^{II} , \quad (1)$$

$$\mathcal{C}_{\mu\nu}^I = \frac{\hbar}{4\pi\Omega} \text{Tr} \left\langle \hat{O}_\mu (\hat{G}^+ - \hat{G}^-) \hat{j}_\nu \hat{G}^- - \hat{O}_\mu \hat{G}^+ \hat{j}_\nu (\hat{G}^+ - \hat{G}^-) \right\rangle_c , \quad (2)$$

$$\mathcal{C}_{\mu\nu}^{II} = \frac{\hbar}{4\pi\Omega} \int_{-\infty}^{E_F} \text{Tr} \left\langle \hat{O}_\mu \hat{G}^+ \hat{j}_\nu \frac{d\hat{G}^+}{dE} - \hat{O}_\mu \frac{d\hat{G}^+}{dE} \hat{j}_\nu \hat{G}^+ - \left(\hat{O}_\mu \hat{G}^- \hat{j}_\nu \frac{d\hat{G}^-}{dE} - \hat{O}_\mu \frac{d\hat{G}^-}{dE} \hat{j}_\nu \hat{G}^- \right) \right\rangle_c dE , \quad (3)$$

where \hat{G}^+ and \hat{G}^- are the retarded and advanced Green functions, respectively, Ω is the unit cell volume, and μ, ν are the Cartesian coordinates. If the generalized conductivity $\mathcal{C}_{\mu\nu}$ stands for the charge conductivity $\sigma_{\mu\nu}$, the generalized current operator \hat{O}_μ stands for the electric current operator \hat{j}_μ , given within the relativistic formalism as [15]

$$\hat{j} = -|e|c\boldsymbol{\alpha} . \quad (4)$$

If $\mathcal{C}_{\mu\nu}$ stands for the spin Hall conductivity $\sigma_{\mu\nu}^z$ (with the spin quantization axis along the z coordinate), then \hat{O}_μ stands for the relativistic spin current density operator \hat{J}_μ^z , given by [14]

$$\hat{J}_\mu^z = \left(\beta \Sigma_z - \frac{\gamma_5 \hat{p}_z}{mc} \right) |e|c\alpha_\mu , \quad (5)$$

where we restrict to the cases $\mu = x, y$. The quantities e, m , and c have their usual meaning, \hat{p}_z is the canonical momentum, $\boldsymbol{\alpha}$ and β are the standard 4×4 matrices occurring in the Dirac formalism, and Σ_z and γ_5 are 4×4 matrices defines as

$$\Sigma_z = \begin{pmatrix} \sigma_z & 0 \\ 0 & \sigma_z \end{pmatrix} , \quad \gamma_5 = \begin{pmatrix} 0 & -I_2 \\ -I_2 & 0 \end{pmatrix} .$$

For more details see, e.g., Refs. 14, 16, and 17.

The angular brackets $\langle \rangle_c$ in Eqs. (2) and (3) indicate averaging over configurations, as is required when investigating alloys. To perform this averaging we employ the coherent potential approximation (CPA). This encompasses the self-consistent determination of the single-site potentials as well as configurational averaging when calculating transport properties. In the latter case one has to include the so-called vertex corrections [18, 19], which account for the difference between a configurational av-

the Kubo-Bastin equation [12] implemented using the fully relativistic multiple-scattering or Korringa-Kohn-Rostoker Green function (KKR-GF) method [13]. Introducing a generalized conductivity $\mathcal{C}_{\mu\nu}$, we can express it as [14]

erage of a product and a product of configurational averages,

$$\langle \hat{O}_\mu \hat{G}^+ \hat{j}_\nu \hat{G}^- \rangle_c - \langle \hat{O}_\mu \hat{G}^+ \rangle_c \langle \hat{j}_\nu \hat{G}^- \rangle_c . \quad (6)$$

When dealing with transport properties, the vertex corrections are crucial to discuss scattering processes at impurities as well as for concentrated alloys [1, 3, 20].

To study how the treatment of the disorder in the host influences calculated transport properties, we additionally did some calculations for which the host was treated as a crystal with artificial atoms, as in the virtual crystal approximation (VCA). Specifically, the host potential was constructed as a weighted average of single-site potentials for Fe and Ni (taken from a CPA calculation for undoped Py) and the corresponding atomic number was taken as a weighted average of Fe and Ni atomic numbers. Permalloy doped with V, Co, Pt, or Au was then treated as in a non self-consistent CPA calculation, where for the host potential we took the potential of the artificial “VCA permalloy crystal” and the dopant potential was taken from a proper CPA calculation. Such a procedure does not represent a good approximation for calculating transport properties, nevertheless, it enables us to highlight the differences arising from treating the host either as a periodic crystal or as a disordered alloy.

B. Dealing with finite temperature effects

Finite temperature effects were included by means of the so-called alloy analogy model [21]: temperature-induced atomic displacements and spin fluctuations are treated as localized and uncorrelated, giving rise to two additional types of disorder that can be described using the CPA. For this approach, the atomic potentials are considered as frozen. Local magnetic moments are as-

sumed to be rigid, i.e., only transversal fluctuations are taken into account.

Atomic vibrations were described using 14 displacement vectors, each of them being assigned the same probability. The lengths of these displacement vectors were set to reproduce the temperature-dependent root mean square displacement $\sqrt{\langle u^2 \rangle}$ as given by the Debye's theory [21]. Displacements for different element types on the same site were taken as identical. The Debye temperature Θ_D was estimated for each composition as a weighted average of Debye temperatures of the constituting elements. Elemental Debye temperatures we used are listed in the Appendix.

Spin fluctuations were described by assuming that the local moments are oriented along pre-defined vectors \hat{e}_f which are isotropically distributed; we allowed for 60 values of the polar angle θ_f and 3 values of the azimuthal angle ϕ_f . The probability x_f of each spin orientation was obtained by relying on the mean-field theory [21]. Analogously to the treatment of the displacements, the probabilities x_f are taken independent on which element occupies a given site.

Setting the probability x_f requires knowing the temperature-dependent Weiss field parameter $w(T)$ [21]. It can be obtained within the mean field theory if one knows the reduced magnetization $M(T)/M(0)$, i.e., the ratio of the magnetization $M(T)$ to the magnetization at $T=0$ K (see Ref. 21 for more details). The reduced magnetization $M(T)/M(0)$ is thus an external input parameter for our calculation. We assumed a modified Bloch form for $M(T)$ according to

$$M(T) = M(0) \left[1 - A \left(\frac{T}{T_C} \right)^{(3/2)} \right], \quad (7)$$

where A is a constant. The Curie temperature T_C for undoped Py can be taken from experiment (865 K). For doped Py we first evaluated the mean-field T_C using exchange coupling constants obtained via the Liechtenstein formula [11, 22, 23] and then subtracted from it the difference between the mean-field and experimental T_C for undoped Py (this difference is 220 K in our case). This approach is consistent with the study of Devonport *et al.* [10] on Cr-doped Py, where a more-or-less constant downward shift between theoretical and experimental T_C can be observed. Finally, we set $A=0.35$ because this leads to a good agreement between the model and experimental $M(T)/M(0)$ curves for Pt-doped Py [9]. A representative selection of the $M(T)/M(0)$ curves obtained thereby is presented in the Appendix.

C. Technical details

The real space representation of the Green function operator \hat{G} was evaluated within the ab-initio framework of spin-density functional theory, relying on the generalized gradient approximation using the Perdew, Burke and

Ernzerhof (PBE) functional [24]. The electronic structure embodied in the underlying effective single-particle Dirac Hamiltonian was calculated in a fully relativistic mode using the spin-polarized KKR-GF formalism [13] as implemented in the SPRKKR code [25]. For the multipole expansion of the Green function, an angular momentum cutoff $\ell_{\max}=3$ was used. The potentials were subject to the atomic sphere approximation (ASA). Self-consistent potentials were obtained employing energy integration on a semicircle in a complex plane using 32 points, the \mathbf{k} -space integration was carried out via sampling on a regular mesh corresponding to 30^3 \mathbf{k} -points in the full Brillouin zone (BZ).

For the V, Pt, and Au dopants, the equilibrium lattice constant a_0 was determined for each dopant concentration by minimizing the total energy. For the Co-doped Py, the conductivities were calculated always for the lattice constant obtained for undoped Py because the variation of a_0 with the Co concentration is very small and thus hardly discernible from the numerical noise. This is not surprising given the mutual positions of Fe, Co, and Ni in the periodic table.

The Kubo-Bastin formulae Eqs. (1)–(3) were evaluated using similar settings as used for self-consistent potentials except for the \mathbf{k} -space integrations for energy points close to the real axis at E_F , where a very dense mesh has to be used. The choice of the \mathbf{k} -mesh is especially crucial for crystalline hosts [14] whereas if the host is an alloy the integrands are smoother and performing the \mathbf{k} -mesh integration is not so difficult. Normally we used 576^3 \mathbf{k} -points in the full BZ at E_F and 288^3 \mathbf{k} -points at the energy point next-nearest to E_F . In case of zero-temperature calculations for undoped Py and for Py doped with Co, where the smoothening effect of alloying may not be so strong, we used 1263^3 \mathbf{k} -points at E_F and 631^3 \mathbf{k} -points at the energy point next-nearest to E_F , to be on the safe side.

III. RESULTS AND DISCUSSION

A. Longitudinal conductivity and AMR

1. Calculation of transport quantities

Doping of Py leads to a decrease of the longitudinal charge conductivity σ_{xx} , as illustrated in Fig. 1 (left). The rate of the decrease depends on the dopant, following the sequence Co–Au–Pt–V. The same sequence characterizes also the dependence of the anisotropic magnetoresistance on the dopant concentration (middle panel of Fig. 1). This is, to a large extent, due to the definition of AMR as

$$\frac{\rho_{zz} - \rho_{xx}}{\rho_{\text{aver}}}$$

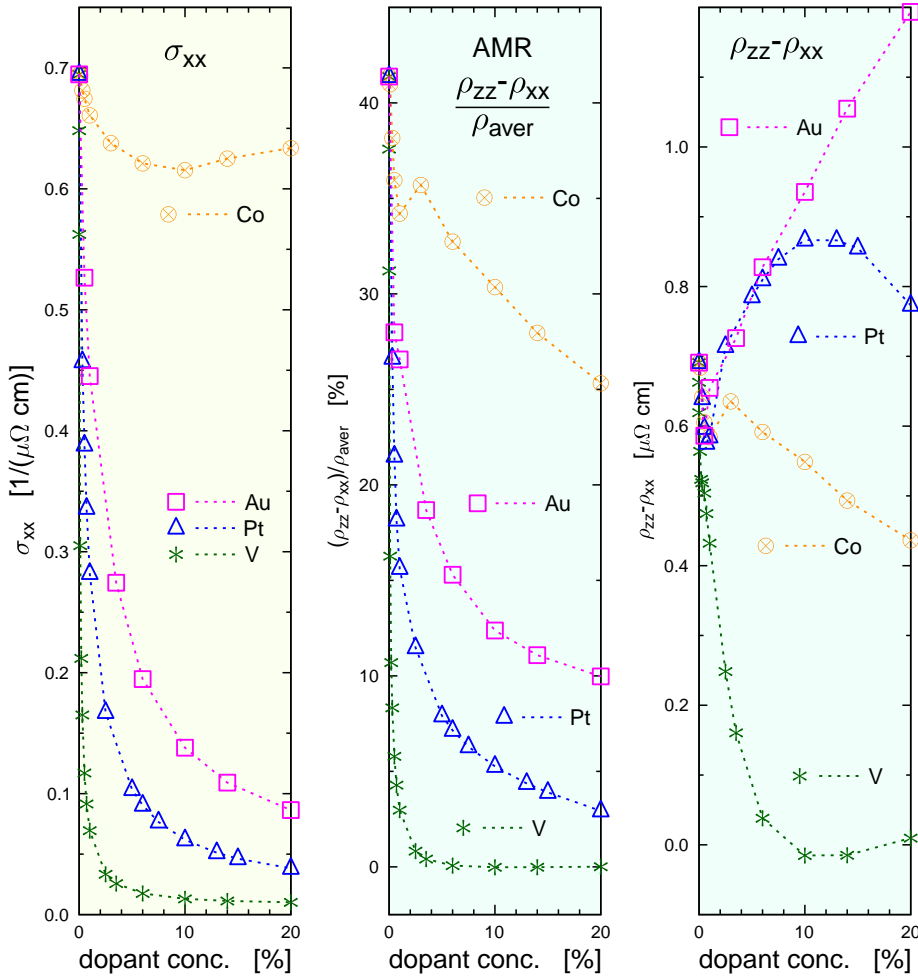


FIG. 1. (Color online) Theoretical longitudinal conductivity σ_{xx} (left), relative anisotropic magnetoresistance $(\rho_{zz} - \rho_{xx})/\rho_{\text{aver}}$ (middle), and the difference of resistivities $\rho_{zz} - \rho_{xx}$ (right) for Py doped with V, Co, Pt, and Au, for $T=0$ K. Calculated values are shown by markers, the lines are guides for an eye. The dopant type is indicated in the legend.

because it is normalized to the average resistance

$$\rho_{\text{aver}} = \frac{1}{3} [2\rho_{xx} + \rho_{zz}] . \quad (8)$$

To provide an uncompensated picture, we show the bare difference $\rho_{zz} - \rho_{xx}$ in the right panel of Fig. 1.

We calculated also spin-resolved conductivities, following the prescription

$$\sigma_{xx}^{(\text{maj})} = \frac{1}{2} (\sigma_{xx} + \sigma_{xx}^z) , \quad (9)$$

$$\sigma_{xx}^{(\text{min})} = \frac{1}{2} (\sigma_{xx} - \sigma_{xx}^z) . \quad (10)$$

We found that practically all the transport is mediated by majority-spin electrons: $\sigma_{xx}^{(\text{min})}$ is by an order of magnitude smaller than $\sigma_{xx}^{(\text{maj})}$ (results not shown). In a two-current model, this would imply a large AMR — see Eq. (6) in Campbell *et al.* [26].

Experimental data are available only for room temperature. Therefore we present in Fig. 2 theoretical results for the average resistivity ρ_{aver} , for the difference between resistivities $\rho_{zz} - \rho_{xx}$, and for the anisotropic magnetoresistance $(\rho_{zz} - \rho_{xx})/\rho_{\text{aver}}$ obtained via the alloy analogy model for $T=300$ K, together with available experimental

data. There is a good overall agreement between theory and experiment of Nagura *et al.* [4] as concerns the average resistivity ρ_{aver} . The agreement is less good for the AMR; the trends are mostly described correctly but there are differences in the absolute values. For Au-doped Py, however, the trends of experimental and theoretical AMR do not agree (middle bottom and right bottom panels in Fig. 2). The experimental AMR data for Pt-doped Py of Hrabec *et al.* [9] exhibit a different trend than the experimental data of Nagura *et al.* [4] and of Yin *et al.* [7], as well as than our theoretical data; the reason for this is unclear.

When assessing the agreement and disagreement between theory and experiment in Fig. 2, one should keep in mind that the experimental data may also be affected by uncertainties, e.g., concerning the concentration of the dopants in the sample or the presence of other defects. Note also that the AMR values obtained by different experiments differ approximately by the same amount as theory and experiment. We conclude that, as a whole, our theoretical data agree with the experimental data presented in Fig. 2 quantitatively as concerns ρ_{aver} and qualitatively as concerns the AMR. We assume that this gives reasonable confidence that our theoretical results

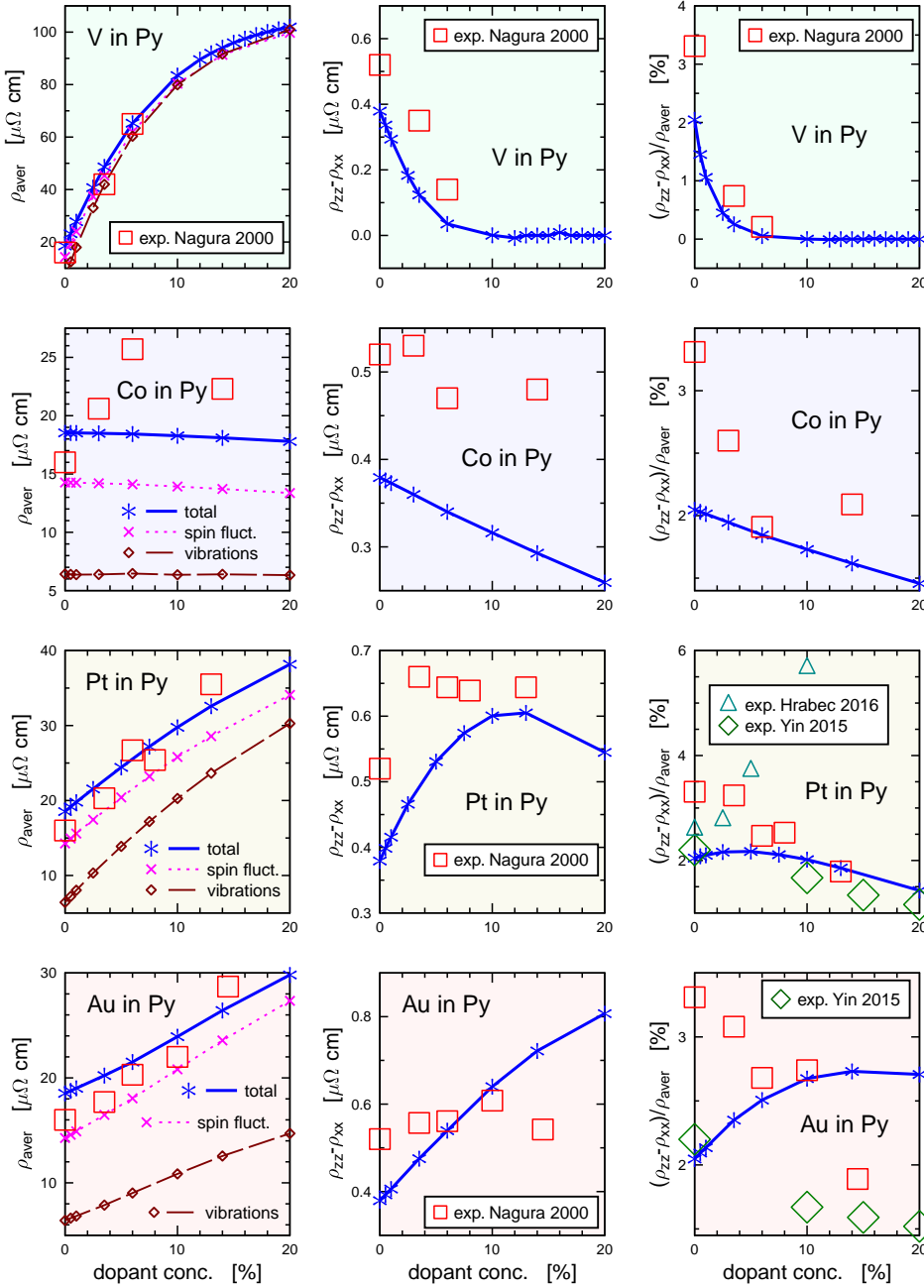


FIG. 2. (Color online) Average resistivity ρ_{aver} , difference between resistivities $\rho_{zz} - \rho_{xx}$, and anomalous magnetoresistance $(\rho_{zz} - \rho_{xx})/\rho_{\text{aver}}$ for Py doped with V, Co, Pt, and Au calculated for $T=300$ K, compared to experiment. Experimental data are from Nagura *et al.* [4], Yin *et al.* [7], and Hrabec *et al.* [9]. For the average resistivity ρ_{aver} , theoretical results obtained when only the spin fluctuations or only the atomic vibrations are accounted for, are also shown.

can be relied on as concerns the general trends and tendencies.

Another test of our calculations can be done for undoped Py by comparing the temperature-dependence of the calculated resistivity ρ_{aver} with available experimental data [28]. This is done in Fig. 3, where the experimental data are shown together with our results and also with calculations of Starikov *et al.* [27], who modeled the temperature-induced disorder by means of supercells. Our calculation of ρ_{aver} accounts quite well for the trend but the agreement with experiment is less good than for the calculations of Starikov *et al.* [27]. A possible reason for this may be the different models used to describe the

thermal disorder by Starikov *et al.* [27] (supercells) and by us (CPA, as outlined in Ebert [21]).

To provide a more specific view on the impact of temperature-induced disorder, data for ρ_{aver} are shown not only for the case when spin fluctuations and atomic vibrations are included together but also when either only the spin fluctuations are included or only the atomic vibrations are included. Note that for the V dopant, the three data sets are hardly distinguishable from each other on the scale of Fig. 2. The contribution to the resistivity due to thermal spin fluctuations,

$$\rho_{\text{aver}}^{(\text{sfluct})}(300 \text{ K}) - \rho_{\text{aver}}(0),$$

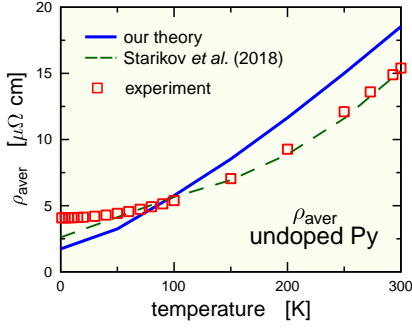


FIG. 3. (Color online) Dependence of the resistivity ρ_{aver} of undoped Py on the temperature as provided by our calculation (blue solid line), by calculations of Starikov *et al.* [27] (green dashed line), and by experiment [28] (red squares).

is typically about three times larger than the contribution due to atomic vibrations,

$$\rho_{\text{aver}}^{(\text{vibr})}(300 \text{ K}) - \rho_{\text{aver}}(0).$$

An exception is the case of V as dopant, for which spin fluctuations dominate for low V concentrations whereas for concentrations larger than about 5 % we found that both contributions are comparable. (This last fact is not discernible on the scale of Fig. 2.)

We checked also the applicability of the Matthiessen rule, i.e., whether the influence of atomic vibrations and of spin fluctuations is additive. The equation

$$[\rho_{\text{aver}}^{(\text{sfluct})}(T) - \rho_{\text{aver}}(0)] + [\rho_{\text{aver}}^{(\text{vibr})}(T) - \rho_{\text{aver}}(0)] = \rho_{\text{aver}}^{(\text{combi})}(T) - \rho_{\text{aver}}(0), \quad (11)$$

with $\rho_{\text{aver}}^{(\text{combi})}(T)$ denoting the resistivity when both spin fluctuations and atomic vibrations are accounted for simultaneously, is always satisfied with an accuracy better than 5 % (typically about 1 %). We checked that this is true also for other temperatures (between 0 K and 300 K). The breakdown of the Matthiessen rule observed for some other systems [21, 29, 30] thus does not occur here.

2. Electronic structure analysis

To get an intuitive insight into the sequence Co–Au–Pt–V which characterizes the efficiency of various dopants in suppressing the high conductivity of Py (see Fig. 1), we inspect how the doping affects relevant aspects of the electronic structure. First, the Bloch spectral function $A_B(\mathbf{k}, E)$ of undoped Py projected on majority-spin and minority-spin states, respectively, is shown in Fig. 4. As it is well-known, the majority-spin states form well-defined bands, demonstrating that the disorder is weak for these states. For minority-spin states, on the other hand, a significant smearing of the bands is evident.

Doping Py with V, Co, Pt, or Au introduces smearing for the majority-spin states as well. From the point of

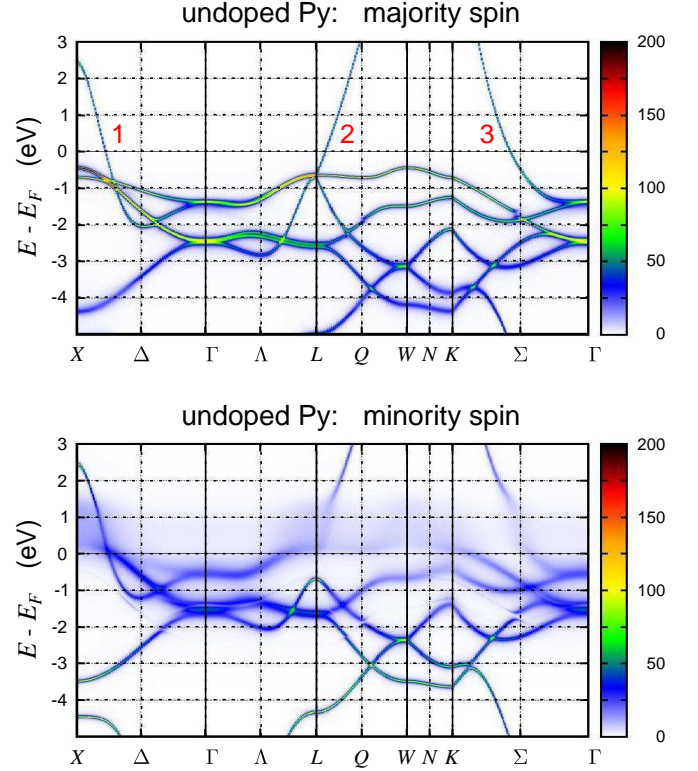


FIG. 4. (Color online) Bloch spectral function $A_B(\mathbf{k}, E)$ of undoped Py projected on majority-spin states and on minority-spin states. Three instances where the majority-spin band crosses the Fermi level are marked by the numbers 1, 2, and 3.

view of transport properties, the most important changes occur around E_F . A detailed view how the doping influences the Bloch spectral function at E_F is presented in Fig. 5. Here, we show majority-spin Bloch spectral function $A_B(\mathbf{k}, E_F)$ for \mathbf{k} in the vicinity of the point marked as 1 in Fig. 4, for Py doped with 1% and 10% of V, Co, Pt, and Au. For the 1% dopant concentration, the changes with respect to the undoped case are relatively small, as to be expected. For the 10% dopant concentration, the changes are obvious. Note that as the spin is not a good quantum number (because of the SOC), the projection of $A_B(\mathbf{k}, E_F)$ on the spin directions cannot be done unambiguously. Namely, it reflects not only the exchange coupling but also the hybridization of spin states. However, our analysis is not really hindered by this.

One can be quantitative and evaluate for each of the peaks in $A_B(\mathbf{k}, E_F)$ the corresponding full width at half maximum (FWHM). We performed this for all three bands which cross the Fermi level in Fig. 4; the results are shown in Table I. Generally, the FWHM's increase if the dopant is varied along the sequence Co–Au–Pt–V. The exception to this rule is the Au–Pt pair in the vicinity of the \mathbf{k} point 1; this deviation is probably due to the SOC.

The FWHM of the Bloch spectral function corresponds to the inverse of the electronic life-time that enters

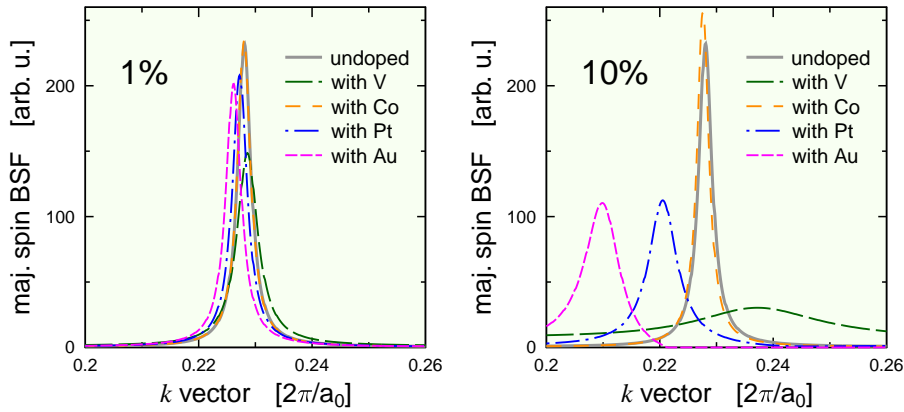


FIG. 5. (Color online) Majority-spin Bloch spectral function at the Fermi level $A_B(\mathbf{k}, E_F)$ for \mathbf{k} in the vicinity of the point marked as 1 in Fig. 4. The \mathbf{k} vector lies on the $X-\Delta$ path, its values are in units of $2\pi/a_0$. The concentration of the dopants is 1% (left) and 10% (right).

TABLE I. FWHM's of peaks (in units of $2\pi/a_0$) of majority-spin Bloch spectral function $A_B(\mathbf{k}, E_F)$ for doped Py if the \mathbf{k} vector is in the vicinity of points marked as 1, 2, and 3 in Fig. 4. Concentration of the dopants is 1% and 10%.

	\mathbf{k} point 1		\mathbf{k} point 2		\mathbf{k} point 3	
	1%	10%	1%	10%	1%	10%
undoped	0.0028		0.0032		0.0039	
Co	0.0028	0.0025	0.0032	0.0031	0.0039	0.0038
Au	0.0033	0.0068	0.0034	0.0054	0.0040	0.0063
Pt	0.0032	0.0061	0.0036	0.0074	0.0046	0.0121
V	0.0045	0.0461	0.0068	0.0611	0.0118	0.1556

the semiclassical theory of electron transport. We also checked the effect of the doping on the slope of the energy band which is linked to the corresponding group velocity. These variations are only few percents (even for 10% doping), with no clear systematic trend. The density of states at E_F , which could be linked to the number of carriers, does not exhibit a systematic trend either and the variations with the doping are less than 10% (corresponding data are not shown). We conclude, therefore, that the decrease of the conductivity of Py upon doping can be traced, first of all, to the decrease of the electron life-time.

For further insight, we analyze in the following the scattering of majority-spin electrons. As the current mediated by minority-spin electrons was found to be practically negligible — see the text below Eq. (10) — we ignore it in this analysis. The lower panel of Fig. 6 depicts the phase-shifts of the majority-spin d electrons (which dominate around E_F) for Fe and Ni host atoms and for V, Co, Pt, and Au impurities. The results we show here were obtained for nominally zero concentrations of the dopants, i.e., for the single-site impurity limit but a similar picture would arise also for finite doping concentrations. One can see that the scattering properties of Co are very similar to those of Fe and Ni in Py, implying that doping Py with Co will influence the transport properties only a little. The influence of V, Pt, and Au, on the other hand, will be much more significant as their atomic scattering properties differ much more from those of the host atoms.

The total cross-section for scattering of majority-spin

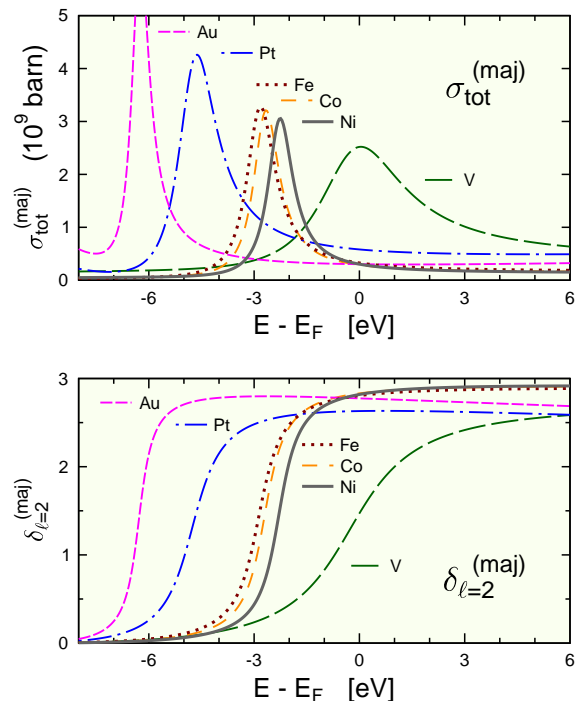


FIG. 6. (Color online) Lower panel: Atomic phase-shifts of majority-spin d electrons for scattering at Fe and Ni as host atoms and at V, Co, Pt, and Au as impurity atoms in Py. Upper panel: Total atomic scattering cross-section of majority-spin electrons for the same types.

electrons $\sigma_{\text{tot}}^{(maj)}$ at each of the atoms (including all angular-momentum components up to $\ell=3$) is shown in the upper panel of Fig. 6. The most significant energy region for transport is around E_F . The corresponding cross-section $\sigma_{\text{tot}}^{(maj)}(E_F)$ decreases in the order V–Pt–Au, in line with the efficiency of these elements to reduce the conductivity of doped Py (cf. left panel of Fig. 1).

One can see this as an illustration that transport properties of doped systems (and compounds and alloys in general) stem from a delicate interplay of the electronic structure of the constituting elements. Vanadium is a 3d element, hence one would expect that its local electronic structure differs less from the electronic structure of Py than the local electronic structure of 5d elements Pt and Au. Consequently, one might assume that V impurities will present a smaller disturbance for transport in Py than Pt or Au impurities. Nevertheless, the V dopants influence the conductivity of Py more than the Pt or Au dopants (Fig. 1). This is clearly because what matters most is the situation at E_F . Fig. 6 shows that the scattering cross-section at V atoms in Py has a peak just at E_F , whereas the cross-sections at Pt and Au atoms in Py have their maxima at lower energies. For other combinations of host and impurity atoms, the situation might obviously be quite different. Seen from another perspective, one can argue that the same mechanism which leads to strong scattering of electrons by V atoms in Py leads also to creation of virtual bound states above E_F for a V impurity in Ni [31].

Finally, let us note that the efficiency of V atoms in reducing the conductivity of Py is *not* directly linked to the antiparallel orientation of magnetic moments of V atoms with respect to moments of host atoms. To check this, we manipulated the local exchange field B_{ex} of V atoms so that it is the same as the average of the exchange fields of the Fe and Ni atoms (and the magnetic moment of V atoms is oriented parallel to the moment of the host atoms). For this situation, the conductivity of V-doped permalloy changes typically by only about 20 % and, accordingly, the overall picture as provided by Fig. 1 remains essentially unchanged.

B. Dependence of AHE and SHE on dopants concentration for $T=0$ K

Off-diagonal conductivities σ_{xy} and σ_{xy}^z calculated for different dopant types are shown in Fig. 7. The dependence of σ_{xy} and σ_{xy}^z on the dopant concentration is highly non-monotonic. Doping with Co introduces only small changes with respect to the undoped case. Doping with Pt and Au — elements with a strong SOC — introduces large changes: even the sign of σ_{xy} or σ_{xy}^z can be reverted in this way. If the dopant concentration approaches zero, values of σ_{xy} and σ_{xy}^z smoothly acquire the values which correspond to undoped Py. Note that this is true also for σ_{xy}^z in the case of the V dopant, even though it is not clearly visible at the scale of Fig. 7:

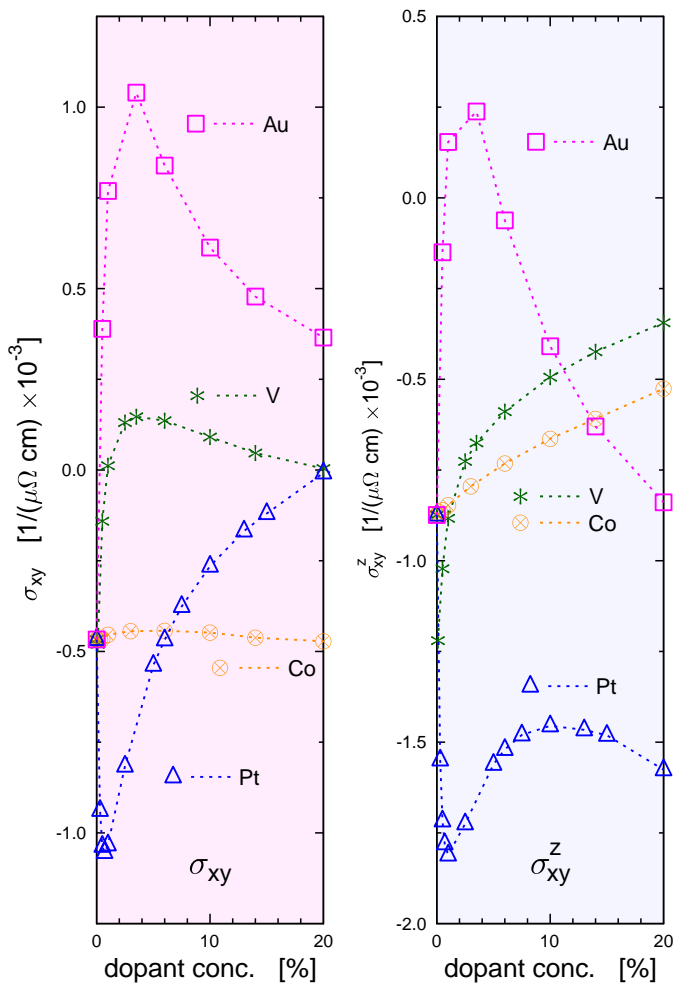


FIG. 7. (Color online) Theoretical off-diagonal conductivities σ_{xy} (corresponding to AHE) and σ_{xy}^z (corresponding to SHE) for Py doped with V, Co, Pt, and Au, for $T=0$ K. Calculated values are shown by markers, the lines are guides for an eye. The dopant types are indicated in the legend.

we verified that σ_{xy}^z has a very sharp minimum for the 0.1% V concentration whereas lowering the doping level further leads to values of σ_{xy}^z which gradually approach the value of σ_{xy}^z of undoped Py. A non-monotonic dependence of σ_{xy} and σ_{xy}^z on the dopant concentration appears to be a general feature for the systems we study.

It has been well-established that σ_{xy} and σ_{xy}^z diverge in the clean limit [20, 32–34]. However, in our case we are not in the clean limit even for zero dopant concentration because the host is not a crystalline metal but a substitutional alloy, with a finite longitudinal conductivity σ_{xx} . Consequently, neither σ_{xy} or σ_{xy}^z diverge at low dopants concentrations, in contrast to the situation for crystalline hosts.

Another feature which highlights the difference between crystalline and disordered host is that, if the dopant concentration is varied, the off-diagonal conductivities σ_{xy} and σ_{xy}^z are not proportional to the longi-

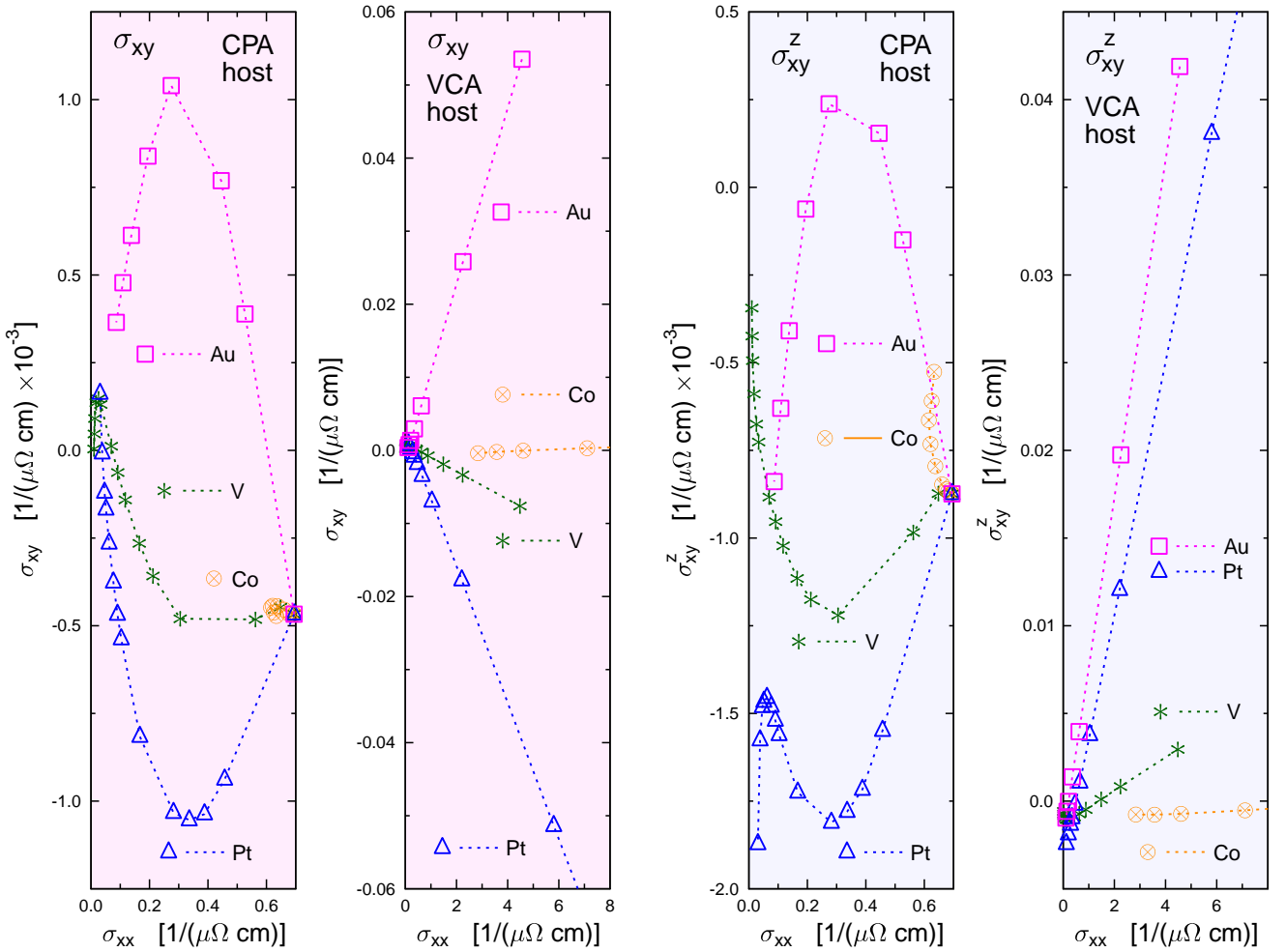


FIG. 8. (Color online) Theoretical dependence of the AHE conductivity σ_{xy} (two left panels) and of the SHE conductivity σ_{xy}^z (two right panels) on the longitudinal conductivity σ_{xx} if the concentration of the dopants is varied (for $T=0$ K). The Py host is treated either within the CPA or within the VCA, respectively, as indicated at the top of the panels. The dopant type is specified in the legend.

tudinal conductivity σ_{xx} for low dopant concentrations, unlike what is common for crystalline hosts [17, 32, 35]. This can be clearly seen in Fig. 8. If the host is treated as a truly disordered system, i.e., within the CPA, the dependence of σ_{xy} and σ_{xy}^z on σ_{xx} is complicated and non-monotonous. Note that different dopants give rise to quite different dependencies of σ_{xy} or σ_{xy}^z on σ_{xx} .

The fact that the host is a disordered system means, among others, that the dependence of the AHE and SHE on the dopant concentration cannot be described unambiguously in terms of skew scattering, side-jump scattering, or intrinsic contribution in the same way as it can be done when investigating the effect of doping for a crystalline host [1, 17, 32, 34, 35]. The above mentioned scheme, namely, assumes that for zero dopant concentration the electron participating in the transport is not scattered. This is true only if the host is a perfect periodic crystal. If the host material is an alloy, the concepts of skew scattering and side-jump scattering can be mis-

leading.

In our theoretical scheme, having a perfect crystal for a host would correspond to treating undoped Py not within the CPA but within the VCA. To illustrate the effect of the host disorder more clearly, we present in Fig. 8 the dependence of σ_{xy} and σ_{xy}^z on σ_{xx} also if the host is treated within the VCA. One can see that in this case both σ_{xy} and σ_{xy}^z depend linearly on σ_{xx} if the dopant concentration is low (i.e., the σ_{xx} conductivity is high). The host disorder thus has a crucial role in the non-monotonic dependence of σ_{xy} and σ_{xy}^z on the dopant concentration (cf. Fig. 7).

It should be noted that the conclusion that the concepts of skew and side-jump scattering are not directly applicable to the analysis of the AHE and SHE in disordered hosts concerns specifically the dependence of σ_{xy} and σ_{xy}^z on the concentration of the dopants. Earlier studies dealing with the mechanism of AHE in fully or partially disordered systems were concerned with the

dependence of AHE either on the thickness of thin film samples [36, 37] or on the degree of partial order [34, 38]. More sophisticated frameworks distinguishing more sources of scattering [39, 40] might be, in principle, applicable to our systems but probably not in a straightforward way: this can be seen, e.g., from the fact that in our case the AHE conductivity σ_{xy} is *not* linearly proportional to σ_{xx} at $T=0$ K, contrary to what formed the basis for earlier multivariable-scaling analyses — cf. Eq. (10) of Yue and Jin [40]. A different approach proposed by Bianco *et al.* [41] uses supercells to describe the disorder and focuses on how it affects the Berry-phase contribution to the AHE, evaluated formally as for an ordered crystal. Despite its conceptual appeal, this approach seems difficult to apply for impurity concentrations of just few percents because of technical issues linked to dealing with large supercells.

Similarly as we did in the case of the longitudinal transport, we also checked the effect of the exchange field B_{ex} on the results. We found that if the local exchange field B_{ex} of the dopant atoms is manipulated so that it is equal to the average of exchange fields of the Fe and Ni host atoms, no significant changes in the calculated values of σ_{xy} or σ_{xy}^z occur (data not shown). The antiparallel orientation of magnetic moment of the V atoms with respect to the host is thus not crucial for longitudinal as well as transverse transport properties of V-doped permalloy.

C. Dependence of AHE and SHE on the temperature

Experiments dealing with electron transport are often done at room temperature. Therefore we present in Fig. 9 the dependence of σ_{xy} and σ_{xy}^z on the concentration of V, Co, Pt, and Au dopants for $T=300$ K, as it follows from the alloy analogy model. This plot should be compared with Fig. 7 where the same dependence is explored for $T=0$ K. It can be seen that the effect of the temperature is really significant: the dependence of σ_{xy} and σ_{xy}^z on the dopants concentration is quite different for $T=0$ K and for $T=300$ K.

A possible reason why the concentration dependencies of σ_{xy} and σ_{xy}^z change so much with temperature is that the vertex corrections [see Eq. (6) and the accompanying text in Sec. II A] become less important when the temperature increases. Intuitively this can be viewed that, in a semi-classical picture, an electron undergoes many scattering events if the temperature is high; there is more disorder, majority-spin electron states lose their crystal-like character, and the differences between various trajectories effectively decrease. All electrons undergo same scattering events in the end, albeit in a different sequence, and the vertex corrections become unimportant. To illustrate this point, we present in Fig. 10 the temperature-dependence of σ_{xy} and σ_{xy}^z for Py doped with 6% of Co and 6% of Au calculated with the vertex corrections either included or omitted. For large enough temperatures

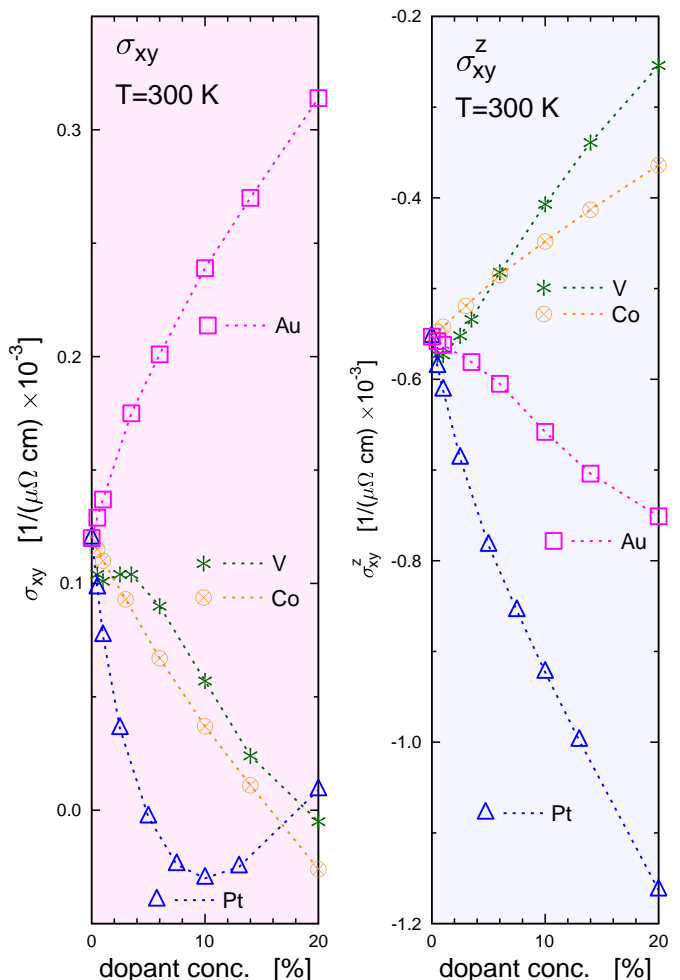


FIG. 9. (Color online) Theoretical off-diagonal conductivities σ_{xy} (corresponding to AHE) and σ_{xy}^z (corresponding to SHE) for Py doped with V, Co, Pt, and Au, for $T=300$ K.

the effect of vertex corrections is getting negligible.

As concerns the longitudinal conductivity σ_{xx} , we checked that the vertex corrections are not important even for zero temperature. In accordance with this, the overall pattern characterizing the dependence of σ_{xx} on the concentration of various dopants for $T=0$ K (Fig. 1) does not change if the temperature increases, even though the numerical values of σ_{xx} obviously decrease if the temperature rises (results not shown).

If the temperature increases, the thermal effects should dominate and, consequently, the differences between various dopings should decrease. This can be seen in Fig. 11, where we present the temperature-dependence of σ_{xy} and σ_{xy}^z for undoped Py as well as for Py doped with 6% of V, Co, Pt, and Au.

The alloy analogy model we employ takes into account atomic vibrations and spin fluctuations together, on the same footing. We can also investigate both effects separately, as it was done for ρ_{aver} in Fig. 2. Illustrative results concerning the temperature-dependence of σ_{xx} ,

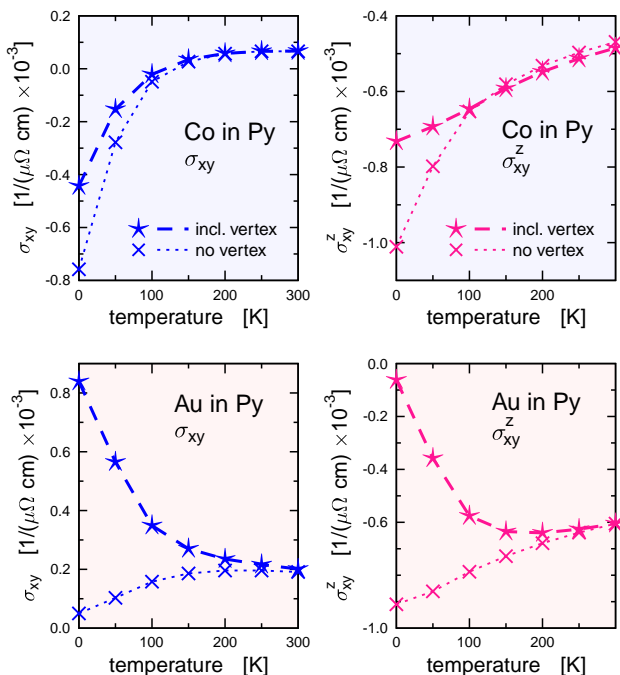


FIG. 10. (Color online) Temperature-dependence of σ_{xy} and σ_{xy}^z for Py doped with 6% of Co and with 6% of Au, calculated for the vertex corrections either included or omitted.

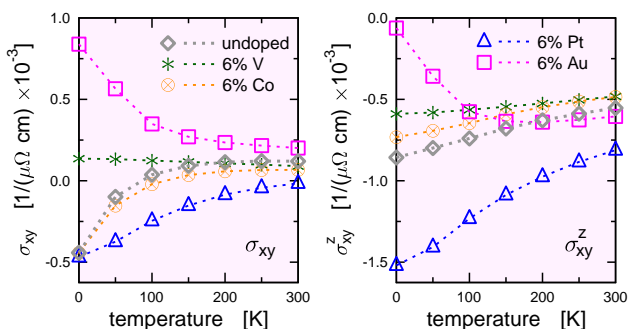


FIG. 11. (Color online) Theoretical temperature-dependence of σ_{xy} and σ_{xy}^z for undoped Py (diamonds) and for Py doped with 6% of V (asterisks), Co (crossed circles), Pt (triangles), and Au (squares).

σ_{xy} , and σ_{xy}^z for Py doped with 6% of V and 6% of Pt are shown in Fig. 12. It seems that there is no universal rule allowing to estimate beforehand which of the two effects — atomic vibrations or spin fluctuations — will be more important for the way the AHE or SHE are affected by the temperature. E.g., the temperature-dependence of σ_{xy} is dominated by atomic vibrations for V-doped Py and by spin fluctuations for Pt-doped Py. We also checked whether the effects of atomic vibrations and of spin fluctuations on the AHE and SHE are additive, i.e., whether the Matthiessen rule Eq. (11) holds also for ρ_{xy} . We found that for V, Co, and Au dopants it is satisfied with the accuracy of about 5 % but for the Pt dopant it

breaks down as the deviations are about 30 %.

As concerns the comparison of our results with experiment, there are only few experimental data available for doped Py. Hrabec *et al.* [9] published data on the anomalous Hall resistivity ρ_{xy} for Pt-doped Py, measured at room temperature. We compare their data with our theoretical results for $T=0$ K and for $T=300$ K in the left panel of Fig. 13. The agreement is worse than for the longitudinal transport (cf. Fig. 2). In particular, our calculations predict a sign-change of ρ_{xy} for room temperature at about 5% concentration of Pt, whereas the data of Hrabec *et al.* [9] do not exhibit this. Also the values of ρ_{xy} themselves differ (albeit they are in the same order of magnitude). It is not clear what can be the reason for this. Let us just note that as concerns the AMR for Pt-doped Py, the experimental data of Hrabec *et al.* [9] differ from the experimental data of Nagura *et al.* [4] and of Yin *et al.* [7].

Calculated temperature-dependence of AHE and SHE resistivities ρ_{xy} and ρ_{xy}^z , respectively, for bulk undoped Py can be compared to experiments done on thin films [42]. The data are shown in the right panel of Fig. 13. Both theory and experiment indicate that the SHE resistivity ρ_{xy}^z varies with temperature much strongly than the AHE resistivity ρ_{xy} . However, despite the general agreement concerning the trends, there are differences between theory and experiment concerning particular values, especially for ρ_{xy}^z at low temperatures. At least part of these differences certainly is due to the fact that the experiment of Omori *et al.* [42] was done for films of 20 nm thickness, meaning that the experimental data reflect also effects due to the finite thickness of the film. In particular, the SHE resistivity ρ_{xy}^z measured at $T=10$ K for a 5 nm-thick film was $-2 \mu\Omega\text{cm}$ whereas for a 20 nm-thick film it was only $-0.3 \mu\Omega\text{cm}$. Conjecturally, further increase of the film thickness would decrease the absolute value of ρ_{xy}^z even further, improving thus the agreement between our theory and experiment. Note that if the temperature increases, the agreement between theoretical and experimental ρ_{xy}^z improves. Presumably, this is because for high enough temperatures the effects of atomic vibrations and spin fluctuations will dominate over surface effects.

D. Relation between AHE and SHE

Both AHE and SHE are spin-dependent transport phenomena related to the SOC, so there is a natural question about their relation. Following an initial suggestion of Tsukahara *et al.* [43], Omori *et al.* [42] argued that within the semiclassical picture and under some specific assumptions, the skew scattering contributions to AHE and SHE conductivities are proportional,

$$\sigma_{xy}^{\text{skew}} = p \sigma_{xy}^{z,\text{skew}}, \quad (12)$$

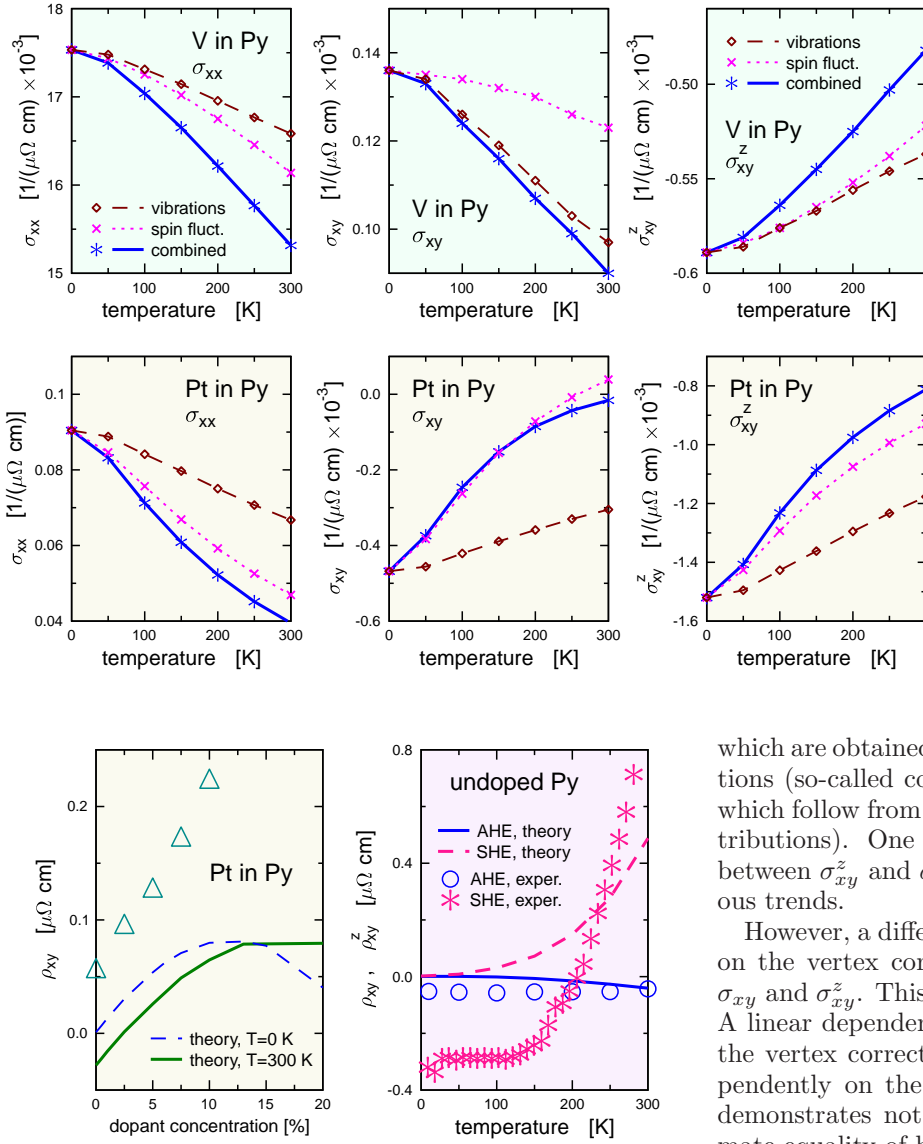


FIG. 13. (Color online) Left: Experimental anomalous Hall resistivity ρ_{xy} for Pt-doped Py measured by Hrabec *et al.* [9] at $T=300 \text{ K}$ (triangles) together with our theoretical data for $T=0 \text{ K}$ (dashed line) and for $T=300 \text{ K}$ (full line). Right: Temperature-dependence of the AHE resistivity ρ_{xy} and the SHE resistivity ρ_{xy}^z for undoped Py obtained from our calculations (lines) and from the experiment of Omori *et al.* [42] (markers). Note that the calculations concern bulk Py while the experiment [42] was done for a thin film.

where p is the spin polarization of the current,

$$p = \frac{\sigma_{xx}^{(\text{maj})} - \sigma_{xx}^{(\text{min})}}{\sigma_{xx}^{(\text{maj})} + \sigma_{xx}^{(\text{min})}}.$$

Exploring the relation between σ_{xy} and σ_{xy}^z for a range of systems like ours might be instructive. Therefore, we present in the left panel of Fig. 14 the SHE conductivity σ_{xy}^z as a function of the AHE conductivity σ_{xy} (for $T=0 \text{ K}$). We include here all contributions, i.e., those

FIG. 12. (Color online) Temperature-dependence of the longitudinal conductivity σ_{xx} and of off-diagonal conductivities σ_{xy} and σ_{xy}^z for Py doped with 6% of V (upper panels) and with 6% of Pt (lower panels). Data are shown separately for calculations where both spin fluctuations and atomic vibrations are accounted for (full lines with asterisks), where only the spin fluctuations are considered (dotted lines with crosses), and where only the atomic vibrations are taken into account (dashed lines with diamonds).

which are obtained without considering the vertex corrections (so-called coherent contributions) as well as those which follow from the vertex corrections (incoherent contributions). One can see immediately that the relation between σ_{xy}^z and σ_{xy} is quite labyrinthine, with no obvious trends.

However, a different picture emerges if one focuses just on the vertex corrections (incoherent contributions) to σ_{xy} and σ_{xy}^z . This is done in the middle panel of Fig. 14. A linear dependence of the vertex corrections to σ_{xy}^z on the vertex corrections to σ_{xy} can be clearly seen, independently on the type of the dopant. In fact Fig. 14 demonstrates not only proportionality but an approximate equality of both quantities,

$$\sigma_{xy}(\text{VC}) = \sigma_{xy}^z(\text{VC}). \quad (13)$$

This relation could be seen as corresponding to Eq. (12), because in our case $p \approx 1$ (see Sec. III A 1). A complementary view on the relation between the vertex correction contributions to σ_{xy} and to σ_{xy}^z is presented in the right panel of Fig. 14. Here we show $\sigma_{xy}(\text{VC})$ and $\sigma_{xy}^z(\text{VC})$ as functions of temperature, for Py doped by 6% of V, Co, Pt, and Au. Again, Eq. (13) is satisfied.

Even though the concept of skew scattering is of limited use (and possibly even misleading) when dealing with changes of the transport properties of Py upon doping (see the discussion accompanying Fig. 8), vertex corrections or, in another terminology, incoherent contributions [44] are robustly defined even for a disordered host. For an ordered host, vertex corrections represent within our approach the skew scattering [32], so we can draw analogies between the relation Eq. (12) suggested by Omori *et al.* [42] for the skew scattering contributions and Eq. (13) satisfied by our data. Vertex corrections are

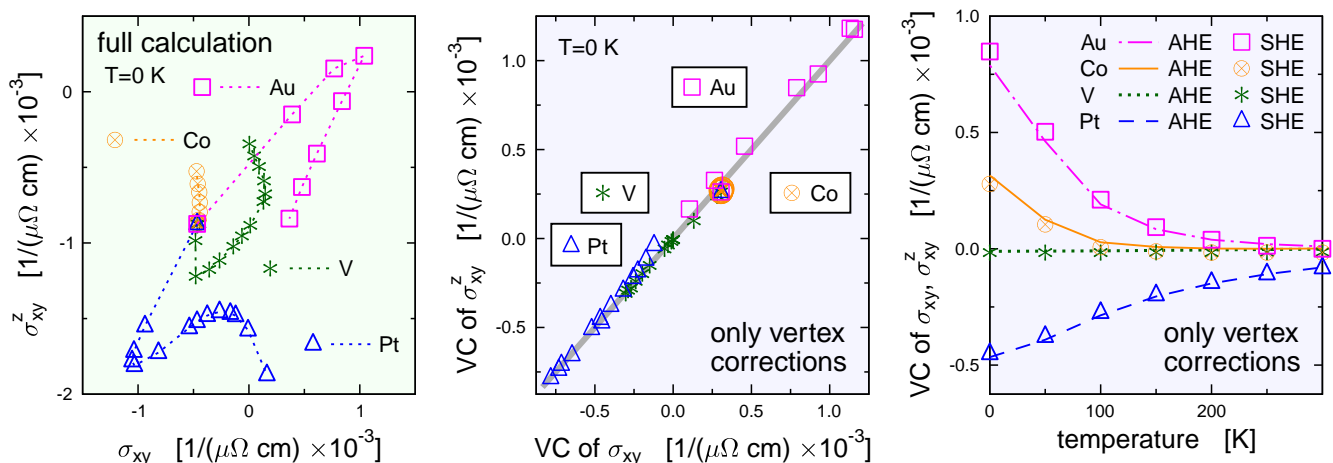


FIG. 14. (Color online) Left: Dependence of the SHE conductivity σ_{xy}^z on the AHE conductivity σ_{xy} for Py doped by V, Co, Pt, and Au (of various concentrations) calculated for $T=0$ K if all contributions to σ_{xy} and σ_{xy}^z are taken into account. Middle: As the left panel but considering only the contributions due to the vertex corrections. The straight line corresponds to the apparent $\sigma_{xy}(\text{VC}) = \sigma_{xy}^z(\text{VC})$ relation. Right: The temperature-dependence of the contributions to σ_{xy} (lines) and to σ_{xy}^z (markers) due to the vertex corrections for Py doped by 6% of V, Co, Pt, and Au.

related to scattering-in terms in the semiclassical Boltzmann transport theory [19], meaning that they reflect extrinsic contributions [42]. For doped Py, their influence on the AHE and SHE is very similar. What makes the AHE conductivity σ_{xy} and SHE conductivity σ_{xy}^z different is thus the coherent or intrinsic contribution.

IV. CONCLUSIONS

Longitudinal charge conductivity σ_{xx} of permalloy decreases with increasing concentration of the V, Co, Pt, or Au dopants. This can be intuitively understood as a consequence of the decrease of free-electron mean-free path deduced from the broadening of the Bloch spectral function at E_F . The rate of the decrease depends on the dopant type, following the sequence Co–Au–Pt–V, in accordance with the scattering properties of each atom type. Experimental data on the longitudinal resistivity ρ_{xx} and on the anisotropic magnetoresistance $(\rho_{zz} - \rho_{xx})/\rho_{\text{aver}}$ at room temperature can be qualitatively reproduced in most cases if the effect of finite temperature is included via the alloy analogy model. For the Au dopant, the theoretical and experimental trends concerning the dependence of the AMR on the dopant concentration disagree.

The calculated dependence of σ_{xy} and σ_{xy}^z on the dopant concentration is found to be non-monotonic and strongly depends on the temperature. The fact that the permalloy host is disordered and not crystalline has profound influence on how σ_{xy} and σ_{xy}^z (characterizing the anomalous Hall effect and the spin Hall effect, respectively) depend on the dopant concentration. In particular, the off-diagonal conductivities σ_{xy} and σ_{xy}^z are not proportional to the longitudinal conductivity σ_{xx} for low dopant concentrations. As a consequence, the depen-

dence of the AHE and SHE on the dopant concentration cannot be ascribed unambiguously to skew scattering, side-jump scattering, or intrinsic contributions in the same way as it can be done when investigating the effect of doping for a crystalline host.

The SHE conductivity σ_{xy}^z for doped permalloy is not proportional to the AHE conductivity σ_{xy} . However, the vertex corrections to σ_{xy}^z are proportional (and, in fact, approximately equal) to the vertex corrections to σ_{xy} . What makes σ_{xy} and σ_{xy}^z of doped Py different is thus the coherent contribution.

Allowing for the impact of finite temperatures dramatically changes the overall trends in the dependence of σ_{xy} and σ_{xy}^z on dopant concentrations. There is no universal rule which of the two effects we consider, namely, atomic vibrations and spin fluctuations, will be more important.

ACKNOWLEDGMENTS

This work was supported by the Czech Science Foundation (GA ČR) via the project 20-18725S and by the Ministry of Education, Youth and Sport (Czech Republic) via the project CEDAMNF CZ.02.1.01/0.0/0.0/15_003/0000358. Additionally, financial support by the DFG via SFB 1277 is gratefully acknowledged.

Appendix: Input data for the alloy analogy model

We present in this appendix the values we used as input for describing finite temperature effects by means of the alloy analogy model (Sec. II B). The Debye temperatures for each element constituting the systems we

TABLE II. Debye temperatures of elements constituting the systems we investigate. Debye temperatures for specific compositions were obtained as weighted averages of the values shown here.

element	Θ_D [K]
Fe	420
Ni	375
V	385
Co	420
Pt	230
Au	170

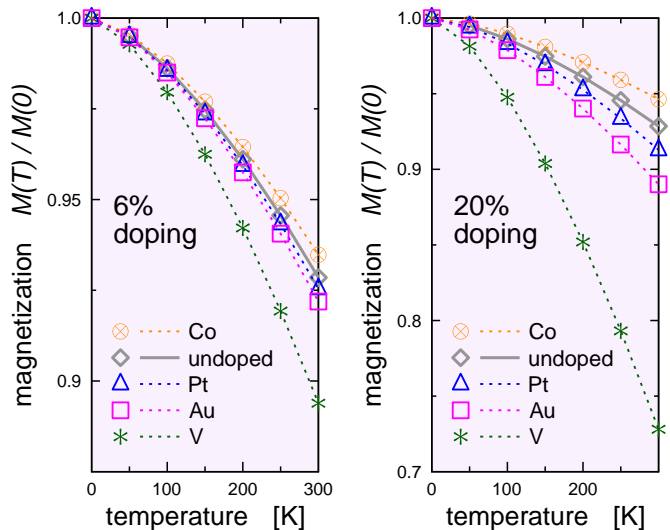


FIG. 15. (Color online) Reduced magnetization $M(T)/M(0)$ used as input for the alloy analogy model. Data are shown for undoped Py and for Py doped by 6% or 20% of V, Co, Pt, and Au.

investigate are presented in Tab. II. The reduced magnetization curves $M(T)/M(0)$ for two representative concentrations of the dopants are shown in Fig. 15.

* sivr@fzu.cz; <http://www.fzu.cz/~sivr>

- ¹ A. Crépieux and P. Bruno, Phys. Rev. B **64**, 094434 (2001).
- ² S. Onoda, N. Sugimoto, and N. Nagaosa, Phys. Rev. Lett. **97**, 126602 (2006).
- ³ N. A. Sinitsyn, J. Phys.: Condens. Matter **20**, 023201 (2008).
- ⁴ H. Nagura, K. Saito, K. Takanashi, and H. Fujimori, J. Magn. Magn. Materials **212**, 53 (2000).
- ⁵ S. Lepadatu, J. S. Claydon, C. J. Kinane, T. R. Charlton, S. Langridge, A. Potenza, S. S. Dhessi, P. S. Keatley, R. J. Hicken, B. J. Hickey, and C. H. Marrows, Phys. Rev. B **81**, 020413(R) (2010).
- ⁶ S. Lepadatu, J. S. Claydon, D. Ciudad, C. J. Kinane, S. Langridge, S. S. Dhessi, and C. H. Marrows, Appl. Physics Lett. **97**, 072507 (2010).
- ⁷ Y. Yin, F. Pan, M. Ahlberg, M. Ranjbar, P. Dürrenfeld, A. Houshang, M. Haidar, L. Bergqvist, Y. Zhai, R. K. Dumas, A. Delin, and J. Åkerman, Phys. Rev. B **92**, 024427 (2015).
- ⁸ F. Pan, J. Chico, J. Hellsvik, A. Delin, A. Bergman, and L. Bergqvist, Phys. Rev. B **94**, 214410 (2016).
- ⁹ A. Hrabec, F. J. T. Gonçalves, C. S. Spencer, E. Arenholz, A. T. N'Diaye, R. L. Stamps, and C. H. Marrows, Phys. Rev. B **93**, 014432 (2016).
- ¹⁰ A. Devonport, A. Vishina, R. Singh, M. Edwards, K. Zheng, J. Domenico, N. Rizzo, C. Kopas, M. van Schilfgaarde, and N. Newman, J. Magn. Magn. Materials **460**, 193 (2018).

- ¹¹ O. Šipr, S. Mankovsky, and H. Ebert, Phys. Rev. B **100**, 024435 (2019).
- ¹² A. Bastin, C. Lewiner, O. Betbeder-Matibet, and P. Nozieres, J. Phys. Chem. Solids **32**, 1811 (1971).
- ¹³ H. Ebert, D. Ködderitzsch, and J. Minár, Rep. Prog. Phys. **74**, 096501 (2011).
- ¹⁴ D. Ködderitzsch, K. Chadova, and H. Ebert, Phys. Rev. B **92**, 184415 (2015).
- ¹⁵ M. E. Rose, *Relativistic Electron Theory* (Wiley, New York, 1961).
- ¹⁶ S. Lowitzer, D. Ködderitzsch, and H. Ebert, Phys. Rev. B **82**, 140402(R) (2010).
- ¹⁷ S. Lowitzer, M. Gradhand, D. Ködderitzsch, D. V. Fedorov, I. Mertig, and H. Ebert, Phys. Rev. Lett. **106**, 056601 (2011).
- ¹⁸ B. Velický, Phys. Rev. **184**, 614 (1969).
- ¹⁹ W. H. Butler, Phys. Rev. B **31**, 3260 (1985).
- ²⁰ J. Sinova, S. O. Valenzuela, J. Wunderlich, C. H. Back, and T. Jungwirth, Rev. Mod. Phys. **87**, 1213 (2015).
- ²¹ H. Ebert, S. Mankovsky, K. Chadova, S. Polesya, J. Minár, and D. Ködderitzsch, Phys. Rev. B **91**, 165132 (2015).
- ²² A. I. Liechtenstein, M. I. Katsnelson, V. P. Antropov, and V. A. Gubanov, J. Magn. Magn. Materials **67**, 65 (1987).
- ²³ M. Pajda, J. Kudrnovský, I. Turek, V. Drchal, and P. Bruno, Phys. Rev. B **64**, 174402 (2001).
- ²⁴ J. P. Perdew, K. Burke, and M. Ernzerhof, Phys. Rev. Lett. **77**, 3865 (1996).
- ²⁵ H. Ebert, *The SPRKKR package version 8*, <http://olymp.cup.uni-muenchen.de/ak/eibert/SPRKKR> (2018).

- ²⁶ I. A. Campbell, A. Fert, and O. Jaoul, *J. Phys. C: Solid State Phys.* **3**, S95 (1970).
- ²⁷ A. A. Starikov, Y. Liu, Z. Yuan, and P. J. Kelly, *Phys. Rev. B* **97**, 214415 (2018).
- ²⁸ C. Y. Ho, M. W. Ackerman, K. Y. Wu, T. N. Havill, R. H. Bogaard, R. A. Matula, S. G. Oh, and H. M. James, *J. Phys. Chem. Ref. Data* **12**, 183 (1983).
- ²⁹ J. K. Glasbrenner, B. S. Pujari, and K. D. Belashchenko, *Phys. Rev. B* **89**, 174408 (2014).
- ³⁰ V. Drchal, J. Kudrnovský, D. Wagenknecht, and I. Turek, *J. Magn. Magn. Materials* **475**, 767 (2019).
- ³¹ N. Stefanou, A. Oswald, R. Zeller, and P. H. Dederichs, *Phys. Rev. B* **35**, 6911 (1987).
- ³² S. Onoda, N. Sugimoto, and N. Nagaosa, *Phys. Rev. B* **77**, 165103 (2008).
- ³³ N. Nagaosa, J. Sinova, S. Onoda, A. H. MacDonald, and N. P. Ong, *Rev. Mod. Phys.* **82**, 1539 (2010).
- ³⁴ K. Hyodo, A. Sakuma, and Y. Kota, *Phys. Rev. B* **94**, 104404 (2016).
- ³⁵ K. Chadova, D. V. Fedorov, C. Herschbach, M. Gradhand, I. Mertig, D. Ködderitzsch, and H. Ebert, *Phys. Rev. B* **92**, 045120 (2015).
- ³⁶ G. Su, Y. Li, D. Hou, X. Jin, H. Liu, and S. Wang, *Phys. Rev. B* **90**, 214410 (2014).
- ³⁷ Y. Li, D. Hou, L. Ye, Y. Tian, J. Xu, G. Su, and X. Jin, *Europhys. Lett.* **110**, 27002 (2015).
- ³⁸ L. J. Zhu, D. Pan, and J. H. Zhao, *Phys. Rev. B* **89**, 220406 (2014).
- ³⁹ D. Hou, G. Su, Y. Tian, X. Jin, S. A. Yang, and Q. Niu, *Phys. Rev. Lett.* **114**, 217203 (2015).
- ⁴⁰ D. Yue and X. Jin, *J. Phys. Soc. Japan* **86**, 011006 (2017).
- ⁴¹ R. Bianco, R. Resta, and I. Souza, *Phys. Rev. B* **90**, 125153 (2014).
- ⁴² Y. Omori, E. Sagasta, Y. Niimi, M. Gradhand, L. E. Hueso, F. Casanova, and Y. Otani, *Phys. Rev. B* **99**, 014403 (2019).
- ⁴³ A. Tsukahara, Y. Ando, Y. Kitamura, H. Emoto, E. Shikoh, M. P. Delmo, T. Shinjo, and M. Shiraishi, *Phys. Rev. B* **89**, 235317 (2014).
- ⁴⁴ I. Turek, J. Kudrnovský, and V. Drchal, *Phys. Rev. B* **89**, 064405 (2014).